This article has been accepted for publication in a future issue of this journal, but has not been fully edited. Content may change prior to final publication. Citation information: DOI 10.1109/TAP.2016.2589958, IEEE Transactions on Antennas and Propagation

Hybrid Model For Reverberant Indoor Radio Channels Using Rays and Graphs

Gerhard Steinböck, Mingming Gan, Paul Meissner, Erik Leitinger, Klaus Witrisal, Thomas Zemen, Troels Pedersen

***Abstract*—Ray-tracing tools allow for deterministic simulation of the channel impulse response. Studies show that these tools work well when the impulse response consists only of a few distinct components. However, measurements of the channel impulse response in indoor environments reveal a diffuse tail. This diffuse tail is difficult to include in ray-tracing due to the computational complexity. We propose a hybrid model to include deterministic components and the diffuse tail by combining ray-tracing with a propagation graph. The recursive structure of the propagation graph allows for a computationally efficient calculation of the channel transfer function considering infinitely many components. We use ray-tracing and the theory of room electromagnetics to obtain the parameter settings for the propagation graph. Thus the proposed hybrid model does not require new or additional parameters in comparison to ray-tracing. Simulation results show good agreement with measurements with respect to the inclusion of the diffuse tail in both the delay power spectrum and the azimuth-delay power spectrum.**

***Index Terms*—Indoor environments, radio propagation, ray-tracing, reverberation.**

I. Introduction

Modeling of radio channel responses is a prerequisite for the simulation and emulation of radio channels. Both stochastic and deterministic models [1] may be applied, depending on the considered system and objective of the simulation. In general, the computational complexity of such simulations depends on the particular channel model. Therefore, to allow for efficient, yet realistic, simulation of radio channels, it is important to select an appropriate modeling technique for the phenomenon under investigation.

In this contribution, we turn our attention to efficient simulation of a phenomenon observed in indoor channel measurements. For measurements with sufficiently large bandwidth the channel impulse response, or rather the power delay profile, appears to consist of a number of narrow peaks with high power and a diffuse component or "diffuse tail" [2]–[9]. The diffuse tail is sometimes called the dense multipath component (DMC) [3]–[7]. Overall, the power appears to drop off exponentially with delay, and generally the high power peaks appear in the early part of the response.

The phenomenon has been studied in great detail in the past two decades and various explanations for the effect have been considered [2]–[9]. The diffuse tail obviously influences the root mean square (rms) delay spread. The relevance of the tail for other parameters in communications, such as directional spread, capacity/mutual information and the channel diversity measure, has been investigated in [3], [4], [6], [10]. These investigations indicate that the tail is typically more important in non-line-of-sight conditions. The impact of diffuse multipath on indoor positioning has been investigated in [11]. These observations have motivated the inclusion of the diffuse tail in several models, e.g. [10], [12] and references therein.

Overall, it is observed that single peaks can be attributed to propagation via specific "paths" through the environment, with limited number of interactions or "bounces". Consequently these components are efficiently modeled and simulated via deterministic methods such as ray-tracing. A superposition of a great many signal components has been considered to simulate an impulse response which includes a diffuse tail [13], [14]. Those components may originate from propagation paths considering specular reflections and scattering [13], [15]–[18]. However, it appears that the tail originates from myriads of components arriving at the receiver after a large number of bounces, see Fig. 1. Thus the tail may be attributed to a reverberation phenomenon as described by the theory of room electromagnetics [8], [9], [19]–[22]. Obviously, modeling of such a scenario using ray-tracing methods, directly, results in a high computational load. Furthermore, the great accuracy with which each component of the diffuse tail is computed may be in vain for simulation purposes, since there we care mostly about the combined effect of the whole diffuse tail.

Combinations of ray-tracing with stochastic models have been proposed to model the channel response. An example is the work in [12] which combines ray-tracing with a stochastic model. Propagation paths obtained from ray-tracing considering specular reflections are associated with a "diffuse multi-path cluster" which is generated stochastically. Another example is the work [23], where ray-tracing is combined with a geometric-stochastic approach that places a certain number of scatterers randomly centered around the interaction points obtained from specular reflection. One common drawback of these methods is that parameter settings for their respective stochastic extensions are obtained by fitting to specific measurements. However, this does not allow to make predictions of dispersion of the diffuse tail in delay and direction for other environments.

G. Steinböck and T. Pedersen are with the Dept. of Electronic Systems, Section WCN at Aalborg University, Denmark. P. Meissner, E. Leitinger and K. Witrisal are with Graz University of Technology, Austria. M. Gan and T. Zemen are with AIT, Austrian Institute of Technology, Vienna, Austria.

The work by G. Steinböck and T. Pedersen was supported by the EU framework of the FP7 Network of Excellence in Wireless COMmunications NEWCOM♯ (Grant agreement no. 318306) and by the cooperative research project VIRTUOSO, funded by Intel Mobile Communications, Anite, Telenor, Aalborg University, and the Danish National Advanced Technology Foundation. The work of P. Meissner, E. Leitinger and K. Witrisal was partly supported by the Austrian Science Fund (FWF) within the National Research Network SISE project S10610. The work by M. Gan was partly supported by the strategic FTW project I-0. This work was also carried out in cooperation within the COST IC1004 Action.

This article has been accepted for publication in a future issue of this journal, but has not been fully edited. Content may change prior to final publication. Citation information: DOI 10.1109/TAP.2016.2589958, IEEE Transactions on Antennas and Propagation

An alternative model proposed in [24] effectively represents the channel impulse responses of reverberant channels as a propagation graph. The recursive structure of the graph allows for a computationally efficient simulation of an infinite number of bounces and represents the diffuse tail well.

These considerations motivate our interest in designing a hybrid model considering both deterministic propagation paths and a diffuse tail. In the present contribution, we propose to combine ray-tracing with the propagation graph to obtain a computationally efficient simulation model. Moreover, we utilize the strength of both models, i.e. ray-tracing provides the deterministic components and the propagation graph generates the diffuse tail. The original work in [24] introduces the propagation graph modeling framework. The work discusses how to represent various stochastic models in the propagation graph framework. Here we build upon the propagation graph model obtained from the geometric stochastic representation in [24]. In comparison to [24], we utilize ray-tracing together with room electromagnetics to obtain all parameter values for the propagation graph from the environment description used for ray-tracing. In particular positions of vertices in the graph are generated deterministically via ray-tracing instead of an originally proposed stochastic placement. This placement strategy aims at a more realistic generation of the directional behavior of the diffuse tail. It mimics the observations described in [2], [10], [25] that the diffuse components are related to or follow the specular components. Furthermore, the decay rate of the diffuse tail is predicted with room electromagnetics [21], [22]. This predicted decay rate is used to set gain values in the propagation graph. The proposed hybrid model does not require additional parameters in comparison to ray-tracing only. The predicted channel responses obtained from the hybrid model show good agreement with measurements. In particular the dispersion in delay and direction of the deterministic peaks and the diffuse tail are well represented.

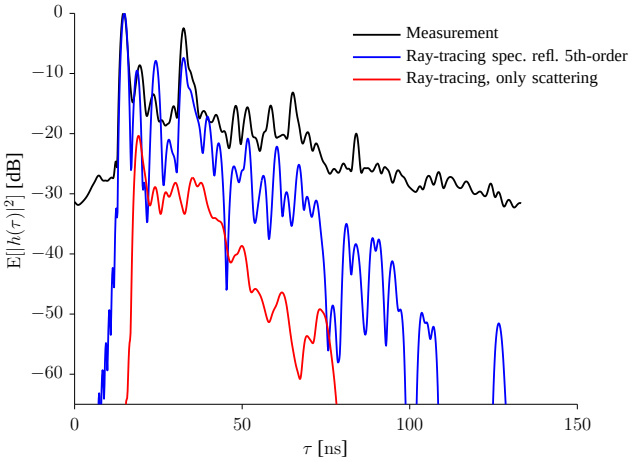

Fig. 1. Measured and simulated delay power spectra from ray-tracing with specular reflections up to fifth-order or scattering. To increase the delay range of scattering we considered first-order scattering, first-order specular reflection followed by scattering and scattering followed by specular reflection as in [10]. The model parameters for diffuse scattering are set according to [26] to the values of $S_{\mathrm{Dif}} = 0.4$ and $\alpha_{\mathrm{Dif}} = 4$ for all materials, except for metal. S_{Dif} and α_{Dif} are the scattering coefficient and the indicator of the scattering lobe width, respectively. A total of ≈ 48000 scattering paths are considered.

II. The Hybrid Model

We consider the case of a time-invariant linear MIMO channel with a (matrix valued) transfer function $\mathbf{H}(f)$. The signal propagates via multiple paths from one of the transmitters to one of the receivers. As in [24] we decompose the transfer function as

$$\mathbf{H}(f) = \sum_{n=0}^{\infty} \mathbf{H}_n(f), \tag{1}$$

where $\mathbf{H}_n(f)$ denotes the contribution of all paths with exactly n interactions. Thus $\mathbf{H}_0(f)$ is the contribution of the line-of-sight (LOS) path and $\mathbf{H}_1(f)$ is the transfer function composed of all paths with single-order interaction. Furthermore, it is convenient to consider the partial responses defined as [24]

$$\mathbf{H}_{K:N}(f) = \sum_{n=K}^{N} \mathbf{H}_n(f). \tag{2}$$

With this definition, we have

$$\mathbf{H}(f) = \mathbf{H}_{0:n_s}(f) + \mathbf{H}_{n_s+1:\infty}(f), \tag{3}$$

where n_s is referred to as the switching order. In cases, where it is not possible or inconvenient to model the two terms by the same method, it seems obvious to use a hybrid approach with one method for the first term and another for the second. In such a hybrid model, the number n_s determines the order of interaction where we switch from one model to the other.

In the case of indoor channels, the first term $\mathbf{H}_{0:n_s}(f)$ may be modeled by ray-tracing for reasonably low n_s. Ray-tracing is, for reasons of computational complexity, not practical to model the second term $\mathbf{H}_{n_s+1:\infty}(f)$ since it accounts for an unbounded number of paths. It is typically not of interest to model the exact behavior of each of these paths as would be done by ray-tracing. It is however important to model the behavior of $\mathbf{H}_{n_s+1:\infty}(f)$ as a whole. Therefore, the second term is modeled by means of a propagation graph which takes into account infinitely many propagation paths. Due to these considerations, we propose a hybrid model with the transfer function defined as

$$\mathbf{H}_{\mathrm{HY}}(f) = \mathbf{H}_{\mathrm{RT},0:\mathrm{n_s}}(f) + \mathbf{H}_{\mathrm{PG},\mathrm{n_s}+1:\infty}(f), \tag{4}$$

where the subscripts HY, RT, and PG refer to the hybrid model, ray-tracing and propagation graph, respectively. The transfer function $\mathbf{H}_{\mathrm{RT},0:\mathrm{n_s}}(f)$ of ray-tracing contains propagation paths of zero-order interaction (LOS) and paths with up to n_{s} interactions (specular reflections, penetration, and diffraction). The transfer function $\mathbf{H}_{\mathrm{PG},\mathrm{n_s}+1:\infty}(f)$ of the propagation graph corresponds to all higher-order interactions and constitutes the diffuse tail. By this way, we simulate the diffuse tail of the overall channel, and not the tail of individual components as in [12], [23].

A. Used Ray-tracing Tool

We base our investigation on a three-dimensional (3D) ray-tracing tool proposed in [10], [27]. Ray-tracing relies on the

This article has been accepted for publication in a future issue of this journal, but has not been fully edited. Content may change prior to final publication. Citation information: DOI 10.1109/TAP.2016.2589958, IEEE Transactions on Antennas and Propagation

description of the geometry and electromagnetic properties of the indoor scenario along with the radiation patterns of the considered antennas. The propagation mechanisms taken into account are: LOS, reflection, penetration, diffraction and scattering. The complex dyadic reflection and penetration coefficients are calculated applying Fresnel formulas [28], while diffraction is implemented using the uniform theory of diffraction (UTD) [29]. The scattering components aim to model reflections on rough surfaces or non-homogenous materials. Scattering can be implemented by dividing the surfaces into multiple tiles, whose sizes are determined by recursively dividing the surface until the far field condition is satisfied for each tile [27], [30]. A directive scattering pattern model, which assumes that the scattering lobe is steered towards the direction of the specular reflection [17], is used to evaluate the amplitude of the diffuse scattering field. Based on the assumption that the scattered rays are incoherent, a uniformly distributed random phase is associated with each scattering ray [10]. However, we consider diffuse scattering only in Fig. 1 to demonstrate that under typical computational restrictions one cannot recreate the diffuse tail[1].

In the hybrid model we limit ray-tracing to only consider LOS, specular reflection, diffraction and penetration propagation mechanisms to obtain the channel transfer function $\mathbf{H}_{\mathrm{RT},0:n_\mathrm{s}}(f)$ for paths up to order n_s. The diffuse tail is generated by the propagation graph described in the next subsection.

B. Propagation Graphs

The model proposed in [24] mimics reverberation effects by means of a directed graph [31], called a propagation graph. In a propagation graph, vertices $\mathcal{V} = \mathcal{V}_\mathrm{t} \cup \mathcal{V}_\mathrm{r} \cup \mathcal{V}_\mathrm{s}$ represent transmitters (in $\mathcal{V}_\mathrm{t}$), receivers (in $\mathcal{V}_\mathrm{r}$) and scatterers (in $\mathcal{V}_\mathrm{s}$). Edges in the graph represent the propagation conditions between vertices. An edge is denoted by an ordered pair of vertices $e = (v, v')$. Thus the edge set $\mathcal{E}$ is a subset of $\mathcal{V} \times \mathcal{V}$. The edge set $\mathcal{E}$ is partitioned into four subsets, i.e. $\mathcal{E}_\mathrm{d}$ the set of transmitter-receiver edges, $\mathcal{E}_\mathrm{t}$ transmitter-scatterer edges, $\mathcal{E}_\mathrm{r}$ scatterer-receiver edges, and $\mathcal{E}_\mathrm{s}$ scatterer-scatterer edges, respectively. Signals propagate via the edges of the graph. Thus, to each edge $e \in \mathcal{E}$ we associate a transfer function $A_e(f)$. For convenience we set $A_e(f) = 0$ for an e being a vertex pair not in $\mathcal{E}$. The transmitter vertices emit a signal into their outgoing edges and the receiver vertices sum up the signals impinging via their ingoing edges. The scatterer vertices sum the signals via their ingoing edges and re-emit this into the outgoing edges. An illustration of the propagation graph can be found in [24].

The transfer function $\mathbf{H}_\mathrm{PG}(f)$ can be derived analytically [24]

$$\mathbf{H}_\mathrm{PG}(f) = \mathbf{D}(f) + \mathbf{R}(f)[\mathbf{I} - \mathbf{B}(f)]^{-1}\mathbf{T}(f), \qquad (5)$$

where the transfer matrices $\mathbf{D}(f)$, $\mathbf{T}(f)$, $\mathbf{R}(f)$ and $\mathbf{B}(f)$ contain the edge transfer functions of $\mathcal{E}_\mathrm{d}$, $\mathcal{E}_\mathrm{t}$, $\mathcal{E}_\mathrm{r}$, and $\mathcal{E}_\mathrm{s}$, respectively. An overview on the construction of the transfer matrices can be found in Appendix A or in more detail in [24]. The expression in (5) is obtained by solving the Neumann series generated by the recursive structure of the graph. In a similar way, expressions for the partial transfer function can be obtained [24]. In this manuscript we consider partial transfer functions accounting for interactions from $n_\mathrm{s}+1$ to infinity:

$$\mathbf{H}_{\mathrm{PG},n_\mathrm{s}+1:\infty}(f) = \mathbf{R}(f)\mathbf{B}^{n_\mathrm{s}}(f)[\mathbf{I} - \mathbf{B}(f)]^{-1}\mathbf{T}(f). \qquad (6)$$

It should be noticed that the full response of the propagation graph in (5) is recovered for $n_\mathrm{s} = 0$ and by adding the edges corresponding to the direct propagation $\mathbf{D}(f)$. This analytic expression of the transfer function allows for an unbounded number of interactions, as it is typically the case when the reverberation effect occurs. This allows us to simulate explicitly the later part of the diffuse tail with the propagation graph.

To use the propagation graph for simulation, we must specify the edge transfer functions. Here we follow the example given in [24], where a geometric position $\mathbf{r}_v$, associated to each vertex $v \in \mathcal{V}$, is used to define the edge transfer function as

$$A_e(f) = \begin{cases} g_e(f)\exp(-j2\pi\tau_e f); & e \in \mathcal{E} \\ 0; & e \notin \mathcal{E}. \end{cases} \qquad (7)$$

where $\tau_e = \|\mathbf{r}_v - \mathbf{r}_{v'}\|/c$ and c is the speed of light. The phases of the complex gains in $A_e(f)$ are solely defined via the edge delays to simplify the multi-antenna case. Otherwise random phases added to the edges as in [24] would require a separate treatment for $e \in \mathcal{E}_\mathrm{t}$ and $e \in \mathcal{E}_\mathrm{r}$. The edge gains $\{g_e(f)\}$ are defined as

$$g_e^2(f) = \begin{cases} \frac{1}{(4\pi f\tau_e)^2}; & e \in \mathcal{E}_\mathrm{d} \\ \frac{1}{4\pi f \mu(\mathcal{E}_\mathrm{t})} \cdot \frac{\tau_e^{-2}}{S(\mathcal{E}_\mathrm{t})}; & e \in \mathcal{E}_\mathrm{t} \\ \frac{1}{4\pi f \mu(\mathcal{E}_\mathrm{r})} \cdot \frac{\tau_e^{-2}}{S(\mathcal{E}_\mathrm{r})}; & e \in \mathcal{E}_\mathrm{r} \\ \frac{g^2(f)}{\mathrm{odi}(e)}; & e \in \mathcal{E}_\mathrm{s} \end{cases} \qquad (8)$$

where $\mathrm{odi}(e)$ denotes the outdegree (number of outgoing edges) of the initial vertex of edge e and for any $\mathcal{E}' \subseteq \mathcal{E}$

$$\mu(\mathcal{E}') = \frac{1}{|\mathcal{E}'|}\sum_{e\in\mathcal{E}'}\tau_e \qquad \text{and} \qquad S(\mathcal{E}') = \sum_{e\in\mathcal{E}'}\tau_e^{-2}, \qquad (9)$$

with $|\cdot|$ denoting cardinality.

With the propagation graph we do not aim to model propagation mechanisms of a single propagation path physically correct as is done in ray-tracing (specular reflection, diffraction, etc.). We only focus on modeling the reverberation phenomenon, i.e. we are concerned with the overall physical propagation mechanisms which lead to the diffuse tail. The propagation graph mimics the reverberation phenomenon with a geometric stochastic approach, since we typically cannot distinguish between specific interactions and propagation mechanisms in the diffuse tail. Thus the edge gains, except for $e \in \mathcal{E}_\mathrm{s}$, in (8) depend on the distance (delay). This leads to partial channel transfer functions of the propagation graph with distance dependent power levels. We aim at power levels similar as in ray-tracing for appropriately combining the partial transfer functions in the hybrid model. Considering this, the

[1]The used parameter values for diffuse scattering are specified in the caption of Fig. 1.

This article has been accepted for publication in a future issue of this journal, but has not been fully edited. Content may change prior to final publication. Citation information: DOI 10.1109/TAP.2016.2589958, IEEE Transactions on Antennas and Propagation

proposed edge gains for $e \in \mathcal{E}_\mathrm{d}$ correspond to Friis' equation with isotropic antennas. In a similar manner the product of the edge gains of $e \in \mathcal{E}_\mathrm{t}$ and $e \in \mathcal{E}_\mathrm{r}$ should resemble Friis equation considering first-order interactions. This would require to sum the distances (delays) from transmitter to scatterer and scatterer to receiver. However, this is not easily achieved in the graph, in particular for higher-order interactions when any $e \in \mathcal{E}_\mathrm{t}$ is connected via $e \in \mathcal{E}_\mathrm{s}$ to any $e \in \mathcal{E}_\mathrm{r}$. Thus we approximate the sum of specific distances by considering the average delays $\mu(\mathcal{E}_\mathrm{t})$ and $\mu(\mathcal{E}_\mathrm{r})$ for the edge delays from transmitter to scatterer and scatterer to receiver. In addition we weigh the edges according to their deviation from the mean of the squared distances to reflect smaller or larger edge delays via the terms $\frac{\tau_e^{-2}}{S(\mathcal{E}_\mathrm{t})}$ and $\frac{\tau_e^{-2}}{S(\mathcal{E}_\mathrm{r})}$. Note that this choice of approximation for the edge gains ensures an appropriate power level of the diffuse tail[2]. The edge gains $e \in \mathcal{E}_\mathrm{s}$ are characterised by the decay rate of the diffuse tail. This allows for a simple approximation of the slope. In comparison to [24], we extend the edge gains to be frequency dependent and approximate them as

$$g^2(f) \approx e^{-\frac{\mu(\mathcal{E}_\mathrm{s})}{T_\mathrm{rev}(f)}}, \tag{10}$$

where $T_\mathrm{rev}(f)$ is a frequency dependent reverberation time which is one of the parameters to be specified. We detail in Section III-C a method to predict $T_\mathrm{rev}(f)$ from the environment description required for ray-tracing. Note that $g(f)$ depends on the average delay between scatterers and thus is a random variable when edges between scatterer vertices are obtained stochastically.

Vertice positions and corresponding edge sets can be generated stochastically as in [24] or as we propose in Section III as a combination of deterministic information from ray-tracing and a stochastic edge set generation.

III. Parameter Settings for the Hybrid Model

We propose a selection of the parameters for the hybrid model such that in comparison to ray-tracing there are only few additional parameters. These parameters are obtained either from ray-tracing results or the theory of room electromagnetics.

A. Settings for Ray-tracing

The geometric and electromagnetic parameters for ray-tracing are given by the considered environment. Note that it is a wide-spread practice in the literature to "refine" parameter settings in ray-tracing, e.g. the considered maximum order of interactions, electromagnetic parameters, etc. by comparison to measurements. Here we avoid this practice since our focus is on testing the prediction capability of the proposed hybrid

[2]We considered to utilize the radar range equation instead of the proposed approach. However, the diffuse tail is a mixture of specular reflections and scattered components, as such the simulated power level of the diffuse tail appears to be too low when considering the radar range equation. Note that in other applications the radar range equation may be better suited.

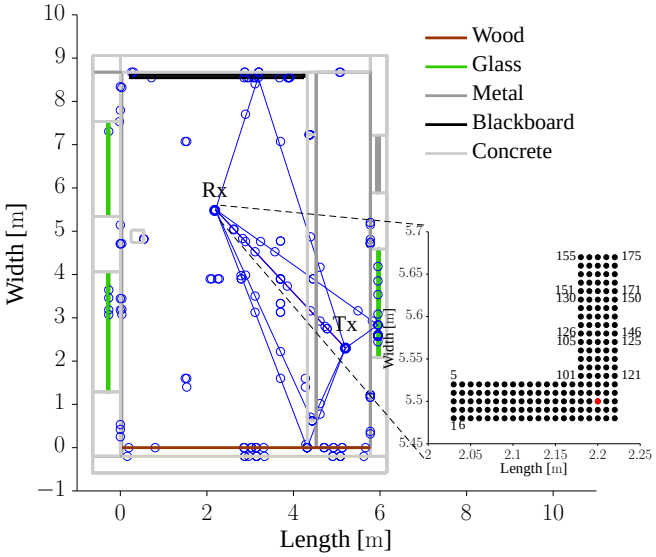

Fig. 2. The considered room with interaction points (blue circles) up to third-order specular reflections obtained from ray-tracing. Line-of-sight and first-order paths are indicated. The considered virtual array with antenna displacement of 1 cm is shown.

(a)

(b)

Fig. 3. The measurement environment shown in (a) from lower right corner and in (b) from upper left corner of the room

This article has been accepted for publication in a future issue of this journal, but has not been fully edited. Content may change prior to final publication. Citation information: DOI 10.1109/TAP.2016.2589958, IEEE Transactions on Antennas and Propagation

TABLE I
PARAMETERS SETTINGS OF THE HYBRID MODEL

Material	ε_r	σ (S/m)	S_i (m^2)	a_i
Concrete	6	0.08	144.36	0.39
Wood	2.1	0.05	18.16	0.46
Glass	5.5	0	15.79	0.4
Metal (PEC)			27.43	0
Mean outdegree $\mathrm{E}[\mathrm{odi}_{\mathcal{V}_\mathrm{s}}]$			5	
Switching order n_s			3	
Reverb. time Eyring $T_\mathrm{rev}(f_c)$			22.9 ns	

model. Instead, we set the electromagnetic parameters according to values from literature [10], [32].

We reconstruct the scenario according to the measurement environment shown in Fig. 2 and Fig. 3. We make a few simplifications in the reconstruction for ray-tracing. One example is the cylindrical pilar shown in Fig. 3a which is reconstructed as a cuboid. The blocks, including doors, walls and pillars, are made of different materials, such as concrete, metal, wood and glass. Metallic blocks, i.e. the radiators, the door, and the blackboard, are considered as a perfect electric conductor (PEC). The values of relative permittivity ε_r and conductivity σ of other materials are presented in Table I. In the simulations the transmitter and receiver antennas are assumed to be ideal omnidirectional dipoles.

B. Setting of the Switching Order n_s

One parameter of the hybrid model, common to ray-tracing and the propagation graph, is the switching order n_s. Typically the computational complexity sets an upper limit to n_s in ray-tracing. However, we consider channel characteristics obtained from ray-tracing such as the simulated received power, mean delay and root mean square (rms) delay spread to select a value for n_s. We select n_s by considering only simulations, i.e. we do not compare to measurements in the selection process. We find the setting for the switching order by increasing n_s until the relative difference between the simulated received power, mean delay and rms delay spread obtained from $\mathbf{H}_{\mathrm{RT},0:n_\mathrm{s}}(f)$ and $\mathbf{H}_{\mathrm{RT},0:n_\mathrm{s}+1}(f)$ are below a certain threshold. This procedure allows us in the hybrid model to stop ray-tracing as soon as the additional contributions are below this threshold.

For the comparison of channel characteristics we consider the discretized channel transfer function obtained from ray-tracing as

$$\mathbf{H}_{\mathrm{RT},0:n,s,a}[i] = \mathbf{H}_{\mathrm{RT},0:n,s,a}(f_c - \tfrac{I-1}{2}\Delta f + i\,\Delta f), \quad (11)$$

where i is the frequency index of I frequency samples separated by Δf in the frequency band centered around f_c. We partition the 175 receive antennas shown in Fig. 2 into seven non-overlapping sub-arrays indexed with s. Each sub-array consists of $A_\mathrm{s} = 5 \times 5$ antennas indexed with a. The received power is obtained for each subarray

$$P_{\mathrm{RT},n,s} = \frac{1}{A_\mathrm{s}} \sum_{a=1}^{A_\mathrm{s}} \frac{1}{I} \sum_{i=0}^{I-1} |\mathbf{H}_{\mathrm{RT},0:n,s,a}[i]|^2, \quad (12)$$

where we average the received power of the antennas within each sub-array to suppress small scale fading. The mean delay $\mu_{\mathrm{RT},n,s}$ and rms delay spread $\sigma_{\mathrm{RT},n,s}$ are the first- and second-order moments of the delay power spectrum

$$P_{\mathrm{RT},n,s}[\ell] = \frac{1}{A_\mathrm{s}} \sum_{a=1}^{A_\mathrm{s}} \left|\mathrm{IDFT}\left\{\mathbf{H}_{\mathrm{RT},0:n,s,a}[i]\, W[i]\right\}[\ell]\right|^2. \quad (13)$$

$\mathrm{IDFT}\{\cdot\}$ is the inverse discrete Fourier transform with respect to i and $W[i]$ denotes a Hann window introduced to reduce sidelobes. $P_{\mathrm{RT},n,s}[\ell]$ is similarly discretized as (11) with $\Delta\tau = \frac{1}{I\,\Delta f}$ and index ℓ. To estimate mean delay and rms delay spread we consider only samples of $P_{\mathrm{RT},n,s}[\ell]$ exceeding $-70\,\mathrm{dB}$[3] from the peak power in $P_{\mathrm{RT},n,s}[\ell]$.

We calculate the ratio of the additional power generated by the nth interaction over the total power as

$$R_{\mathrm{P},s}(n) = \frac{P_{\mathrm{RT},n,s} - P_{\mathrm{RT},n-1,s}}{P_{\mathrm{RT},n,s}}. \quad (14)$$

In a similar manner as (14) we calculate the ratios $R_{\mu,s}(n)$ and $R_{\sigma,s}(n)$ for the mean delay and the rms delay spread, respectively. For the choice of the switching order n_s, we consider a threshold of 1% (or $-20\,\mathrm{dB}$) to be an appropriate choice.

The results of this simulation study are shown in Fig. 4 and summarized here. We observe a sharp increase of the rms delay spread up to order three. After that stabilizes the rms delay spread quickly. A variation of approx. $2\,\mathrm{ns}$ is observed among subarrays as fading is not entirely removed by the spatial averaging procedure. As expected from the observed rms delay spread values, the ratio $R_{\sigma,s}(n)$ has large values at lower order of interactions and decreases quickly. The trends of received power and mean delay are similar to the rms delay spread, however their respective ratios are clearly below $-20\,\mathrm{dB}$ from third-order interactions onwards. Therefore, we omit presenting these figures. Note that we simulate up to fifth-order of interactions to illustrate the trend of the channel characteristics and provide the reader with a better intuition even though the threshold is already achieved earlier. For the received power we observe that the LOS component carries a large portion of the total power. The total power increases only marginally. The total change is approx. $2.2\,\mathrm{dB}$ from LOS only to fifth-order interaction. The mean delay and the rms delay spread, which characterize the delay dispersion, are more sensitive to the order of interaction than the received power. However, as mentioned and shown in Fig. 4, only the rms delay spread appears to provide relevant ratios for higher-order interactions. Considering the impact of increasing order on the estimated rms delay spread values, we observe in Fig. 4b that the change is similar or less than the variation among sub-arrays from third-order onwards. Thus the

[3]In the simulation study to obtain n_s we are not limited by measurement noise. Thus we choose this large dynamic range to include as well weaker components. One of our previous simulation studies for reverberant models has shown that dynamic ranges $> 30\,\mathrm{dB}$ are required such that the estimated rms delay spread coincides with the theoretical value, namely the decay rate of a "simulated" exponentially decaying tail.

This article has been accepted for publication in a future issue of this journal, but has not been fully edited. Content may change prior to final publication. Citation information: DOI 10.1109/TAP.2016.2589958, IEEE Transactions on Antennas and Propagation

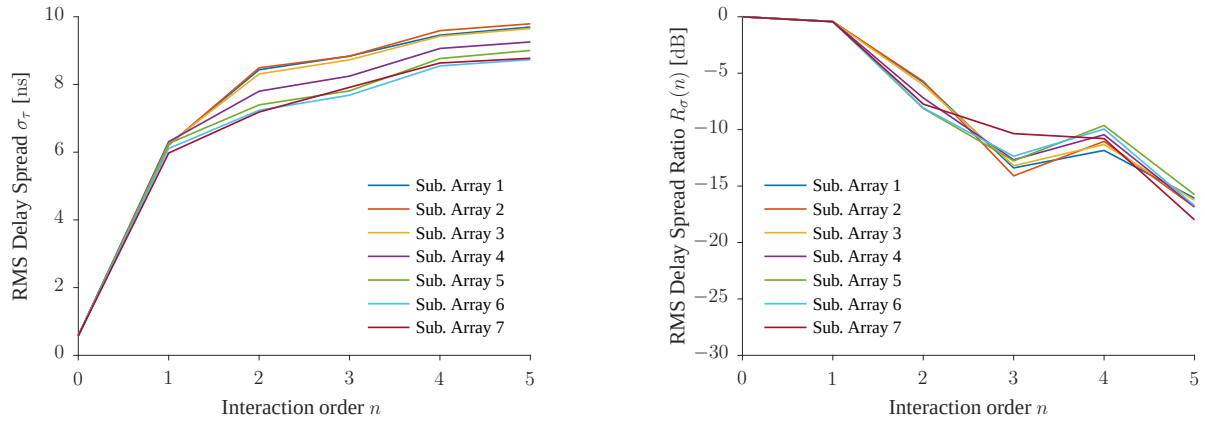

Fig. 4. Rms delay spread (a) for different number of interactions simulated by ray-tracing. The ratio of additional rms delay spread is shown in (b) for various number of interactions. The assumed threshold of 1% corresponds to -20 dB.

additional contributions appear to be marginal with increasing order of specular interaction in ray-tracing and cannot account for the observed diffuse tail.

Considering these results, we choose in our particular case $n_\mathrm{s} = 3$ for the hybrid model. Note that this is not a general value to be considered for all environments, however a simulation study with ray-tracing, as proposed here, can be used to find the appropriate value.

C. Settings for the Propagation Graph

1) Position of Vertices: The positions $\mathbf{r}_v$ of scatterer vertices $\mathcal{V}_\mathrm{s}$ in the graph are obtained from the set of interaction points calculated by ray-tracing. This inherently defines $|\mathcal{V}_\mathrm{s}|$. We focus on the first and last interaction points of the propagation paths since these characterize the main features of the directional power spectra seen from the transmitter and receiver. Note that this keeps the number of scattering vertices low and thus the size of matrix $\mathbf{B}(f)$ small, in particular for $n_\mathrm{s} > 2$. This is beneficial for the computational complexity as $\mathbf{B}(f)$ needs to be inverted. Fig. 5 indicates a few propagation paths originating from first- to third-order specular reflections, together with the interaction points on the walls of a rectangular room. These interaction points are obtained from ray-tracing for antenna position 88, indicated in Fig. 2 by the red dot. All 175 receive antennas are considered as receiver vertices in the propagation graph.

2) Edge Sets: The edge set $\mathcal{E}_\mathrm{t}$ is obtained from ray-tracing and contains the edges from the transmit vertices to the scattering vertices corresponding to the first interaction points, see Fig. 5. Similarly the edge set $\mathcal{E}_\mathrm{r}$ contains all the edges from the subset of scattering vertices corresponding to the last interaction points to the receiver vertices. $\mathcal{E}_\mathrm{r}$ is created for all receive vertices according to ray-tracing results of antenna position 88. Choosing edges in $\mathcal{E}_\mathrm{s}$ deterministically requires a large number of visibility checks, i.e. $|\mathcal{V}_\mathrm{s}|(|\mathcal{V}_\mathrm{s}| - 1)$. For the purpose of generating the diffuse tail it is computationally simpler to interconnect scattering vertices stochastically as

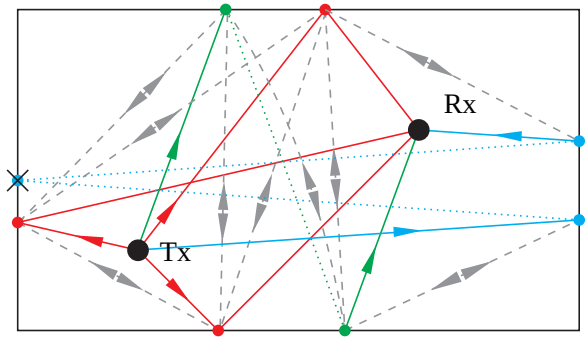

Fig. 5. Representation of the edges of the graph. Some of the first, second and third-order interaction points obtained from ray-tracing are included in red, green, and blue, respectively. Solid and dotted lines correspond to parts of paths obtained from ray-tracing which, respectively, are used or not used in the propagation graph. We only consider the first and last interaction points thus the crossed out interaction point of the third-order propagation path is not part of the graph. Dashed lines indicate edges with probability of visibility P_vis. The double arrows graphically indicate edges in both directions. For clarity we omit some possible edges.

in [24]. In this case, edges in $\mathcal{E}_\mathrm{s}$ are drawn independently with probability P_vis, see the grey dashed edges in Fig. 5. Furthermore, we apply the additional restriction that we do not allow edges between vertices on the same surface.

As shown in Appendix B, the choice of P_vis controls, via the mean outdegree $\mathrm{E}[\mathrm{odi}_{\mathcal{V}_\mathrm{s}}]$ of scatterer vertices the rate by which signal components arrive at the receiver. In particular, if $\mathrm{E}[\mathrm{odi}_{\mathcal{V}_\mathrm{s}}] = (|\mathcal{V}_\mathrm{s}| - 1)P_\mathrm{vis} > 1$ the rate will increase exponentially with the number of interactions. Oppositely, for $\mathrm{E}[\mathrm{odi}_{\mathcal{V}_\mathrm{s}}] < 1$, the rate decreases exponentially. Thus, motivated by this direct impact on the rate, we follow the approach to specify the mean outdegree and use this to set P_vis. We observe by (10) that $\mathrm{E}[\mathrm{odi}_{\mathcal{V}_\mathrm{s}}]$ can be set without affecting the power decay of the tail. Therefore, the power decay exponent and the arrival rates may be adjusted independently. From our experience, the setting of $\mathrm{E}[\mathrm{odi}_{\mathcal{V}_\mathrm{s}}]$ is not overly critical with respect to generating a diffuse tail. With that in mind, we take the simplistic approach to set $\mathrm{E}[\mathrm{odi}_{\mathcal{V}_\mathrm{s}}] = 5$,

This article has been accepted for publication in a future issue of this journal, but has not been fully edited. Content may change prior to final publication. Citation information: DOI 10.1109/TAP.2016.2589958, IEEE Transactions on Antennas and Propagation

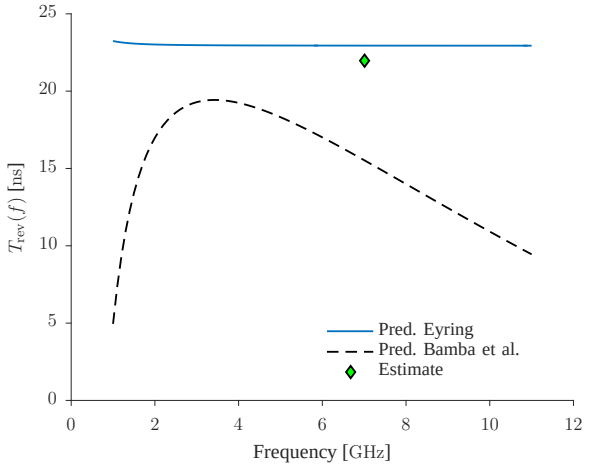

Fig. 6. Predicted reverberation time $T_{\mathrm{rev}}(f)$ considering the proposed method with Eyring's model and the empirical model by Bamba et al. [33]. The estimated reverberation time for the considered center frequency and bandwidth is included. This value and similar not shown estimates for other center frequencies are close to our predicted value and do not show the frequency dependency predicted by Bamba et al. [33].

corresponding to assuming a room with 6 plane walls and that a scatterer vertex placed on one wall can see one scatterer at each of the other walls. However, for some applications where accurate modeling of the arrival rate is needed a more careful setting of this parameter could be considered.

3) Edge Gains: The edge gains for $e \in \mathcal{E}_{\mathrm{d}}$, $e \in \mathcal{E}_{\mathrm{t}}$, and $e \in \mathcal{E}_{\mathrm{r}}$ are specified in (8). The edge gains $e \in \mathcal{E}_{\mathrm{s}}$ are obtained from (10) with a predicted value of the reverberation time. We obtain this predicted value by utilizing room electromagnetic models [8], [9], [19], [20] which we detail in the following.

The reverberation time can be predicted using reverberation models, e.g. by Sabine [34] or Eyring [35]. The input parameters of these models are the volume, surface area and average absorption coefficient of the room. Results in [19] indicate that for room electromagnetics the average absorption coefficient is typically in a range where Eyring's model predicts the reverberation time more accurately than Sabine's. Thus we focus on Eyring's model [35] which predicts the reverberation time as

$$T_{\mathrm{rev}}(f) = \frac{-4\,V}{c\,S\,\ln(1-\bar{a}(f))} \tag{15}$$

with the room volume V, total surface area

$$S = \sum_i S_i, \tag{16}$$

considering surface i with area S_i, speed of light c and average room absorption coefficient

$$\bar{a}(f) = \frac{\sum_i S_i\, a_i(f)}{S}. \tag{17}$$

We predict the average absorption coefficient of the different surface areas by the method proposed in [21], [22] relying on the electromagnetic properties of the materials. For surface i we obtain the average absorption coefficient by averaging the specular reflection coefficients over all incoming angles θ as:

$$a_i(f) = \int_0^{\frac{\pi}{2}} (1 - \tfrac{1}{2}(|\Gamma_{\mathrm{h},i}(\theta,f)|^2 + |\Gamma_{\mathrm{v},i}(\theta,f)|^2)) \cos(\theta)\sin(\theta)\mathrm{d}\theta. \tag{18}$$

The plane wave reflection coefficients for horizontal and vertical polarization, denoted as $\Gamma_{\mathrm{h},i}(\theta,f)$ and $\Gamma_{\mathrm{v},i}(\theta,f)$, are calculated according to the Fresnel formulas [28]. The integral in (18) is solved numerically for all materials in the room considering their respective electromagnetic properties.

Note that Eyring derived his model under the assumption of specular reflections using the mirror theory for different room shapes, e.g. spherical, cylindrical, cuboid. Thus reconstructing for ray-tracing a specific room with all its material properties allows to predict the exponential decay rate. We calculate the respective absorption coefficients based on the materials' relative permittivities and conductivities using (18) and report in Table I their total visible surface areas. With these parameters we predict the reverberation time using Eyring's model (15) versus frequency. As shown in Fig. 6, the proposed prediction method of $T_{\mathrm{rev}}(f)$ shows practically no frequency dependency in the considered frequency band. Thus we consider $T_{\mathrm{rev}}(f)$ to be constant in our simulations and evaluate it at f_c. This is different to the empirical model by Bamba et al. [33] for $T_{\mathrm{rev}}(f)$, which shows a clear frequency dependency (see Fig. 6).

Not shown here, we conducted a similar investigation as in [33] to estimate $T_{\mathrm{rev}}(f)$ for sub-bands filtered with a Hann window (500 MHz bandwidth). The center frequencies of the sub-bands are chosen to cover the total measurement bandwidth. The estimated reverberation times from our measurement data do not agree well with the frequency dependency predicted by [33]. Although the estimates vary over the entire measurement bandwidth and are typically below our predictions, a frequency flat model appears to be more appropriate for our data. The discrepancy between our estimates, the proposed prediction method and the empirical model by Bamba et al. [33] may be due to the frequency dependency of materials in the different environments. Note that frequency dependent material properties, if available, can be readily included in the proposed prediction method. The proposed hybrid model can easily accommodate such a frequency dependency in case this is found necessary for other propagation scenarios.

IV. Measurement Setup

We use a subset of the measurements reported in full detail in [36] to validate the proposed hybrid model. The considered measurements were obtained with a single antenna at the transmitter and a virtual planar array at the receiver in a room with dimensions $6.2\ \mathrm{m} \times 9.5\ \mathrm{m} \times 3.5\ \mathrm{m}$, see Figs. 2 and 3. The virtual array consists of 175 grid points with $1\,\mathrm{cm}$ spacing as shown in Fig. 2. Self-made dipole-like antennas, made of Euro-cent coins have been used at the transmitter and receiver. These antennas have an approximately uniform

This article has been accepted for publication in a future issue of this journal, but has not been fully edited. Content may change prior to final publication. Citation information: DOI 10.1109/TAP.2016.2589958, IEEE Transactions on Antennas and Propagation

TABLE II
SETTINGS OF THE MEASUREMENTS AND THE POST PROCESSING

Measurement	Value
Transmit power	18 dBm
Chip clock rate	6.95 GHz
Chip sequence length in samples	4095
Full measurement bandwidth	3.1 GHz to 10.6 GHz
Maximum excess delay	589.2 ns
Post processing	**Value**
Carrier frequency f_c	7 GHz
Pulse width T_p of Hann pulse	2 ns
Number of Tx antennas N_Tx	1
Number of Rx antennas N_Rx	175

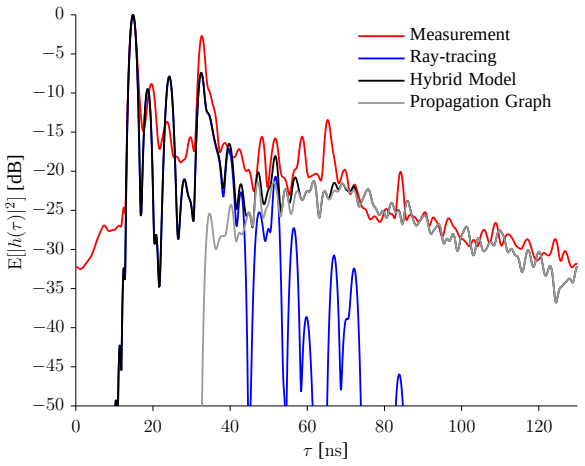

Fig. 7. Measured and simulated delay power spectra. Around 120 ns the contribution of the noise in the measurements is clearly visible in the change of the slope in comparison to the noise-free simulations.

radiation pattern in the azimuth domain and zeroes in the direction of floor and ceiling.

The channel was measured with a UWB channel sounder developed by *Ilmsens* as described in [37], [38]. The measurement principle is correlative channel sounding. A binary code sequence with suitable autocorrelation properties (a large peak-to-off-peak-ratio) is transmitted over the channel. At the receiver, the channel impulse response is recovered by correlation with the known code sequence. Transfer functions of connectors, cables, and the device itself have been calibrated out. The transmit and receive antennas are considered to be part of the propagation channel. A static environment has been ensured during the measurements, i.e. there have been no moving persons or objects. In the postprocessing, we select a frequency band with center frequency f_c and bandwidth $B = 1/T_\mathrm{p}$ by filtering with a Hann pulse with pulse duration T_p. Details on these parameters can be found in Table II.

One characteristic of this particular measurement system is that the measured responses are not obtained in absolute powers. The measurement data is normalized such that the early and strongest peak in delay power spectrum, corresponding to the line of sight path, is unity. The same normalization is done for the simulated data for easy comparison.

TABLE III
ESTIMATES FROM MEASUREMENTS AND SIMULATIONS OF RAY-TRACING CONSIDERING ONLY LOS, UP TO THIRD-ORDER AND THE HYBRID MODEL.

Estimates	RT_0	$\mathrm{RT}_{0:3}$	Hybrid	Meas.
Power Ratio $\frac{P_\mathrm{Sim}}{P_\mathrm{Meas}}$	0.38	0.63	0.69	–
Mean delay μ [ns]	–	20.2	24.6	28.7
Rms delay spread σ [ns]	–	8.2	16.7	17.35

V. RESULTS

In the following we present the simulation results predicted by the hybrid model and compare them to the measurements. In particular we focus on the delay power spectra and the azimuth-delay power spectra. The measurement bandwidth was reduced to fulfill the narrowband array assumption and to apply a conventional Bartlet beamformer to estimate the azimuth-delay power spectra. For details on the estimation procedure see Appendix C.

Fig. 7 shows the measured and simulated delay power spectra, obtained by averaging over the 175 receive antennas. From these delay power spectra we estimated values for the mean delay and rms delay spread. We consider a threshold of -30 dB from the peak power due to noise limitations in the measurements. These estimates are reported in Table III together with the power ratio of simulated power over measured power. The power is estimated similar as in (12), except we consider the average over all antennas. Note that our particular normalization to the line of sight propagation path allows for such a comparison.

Azimuth-delay power spectra obtained from measurements and simulations are shown in Fig. 8. The figures also include the azimuth of arrival angles and the delays for the propagation paths obtained with ray-tracing. The result of the hybrid model is shown in Fig. 8b, which is achieved from the partial responses of ray-tracing and the propagation graph in Fig. 8c and Fig. 8d, respectively.

We do not provide estimates of the rms azimuth spread. High sidelobes from the beamformer strongly influence the results. The high sidelobes are due to the particular geometry of the used array. The sidelobes can be seen in the azimuth-delay power spectra considering the LOS component (indicated with a black circle around the cross) in Fig. 8. At a delay of approx. 15 ns we observe the main lobe at approx. $-45°$. Multiple peaks from sidelobes are observed just around these $-45°$. Due to the array geometry the sidelobes do not roll off and thus we see strong peaks at approx. $-130°$ and $40°$ as well.

VI. DISCUSSION

The delay and azimuth-delay power spectra estimated from the measurements show some low power contributions prior to the LOS component in Fig. 7 and Fig. 8a, respectively. These contributions are possibly caused by insufficient calibration data. We consider these contributions as negligible for our investigations.

This article has been accepted for publication in a future issue of this journal, but has not been fully edited. Content may change prior to final publication. Citation information: DOI 10.1109/TAP.2016.2589958, IEEE Transactions on Antennas and Propagation

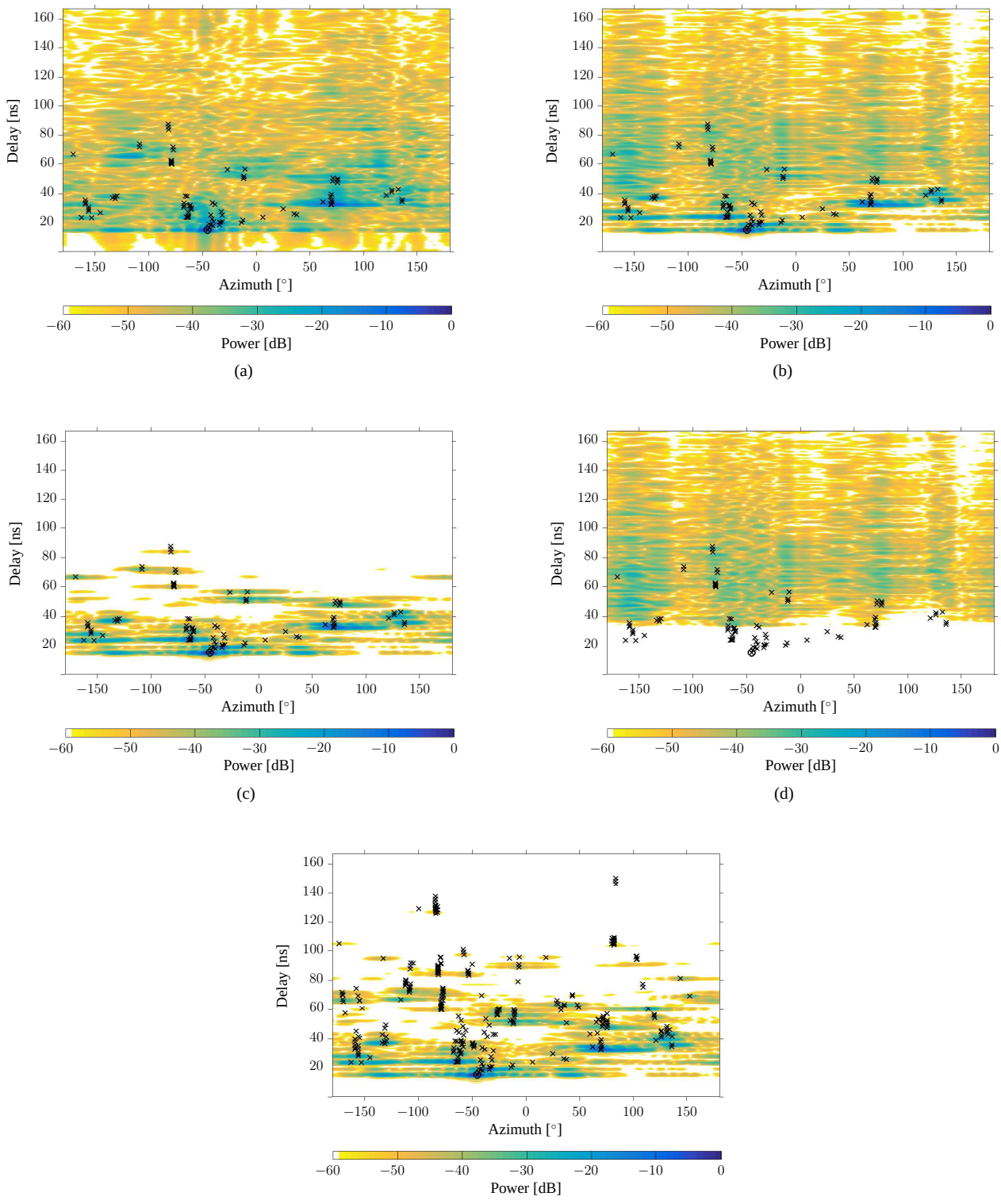

Fig. 8. Azimuth-delay power spectra from measurements (a) and models (b)-(e). The azimuth-delay power spectra of the different subfigures are shown for (b) the hybrid model as $\mathbf{H}_{\mathrm{RT},0:3}(f) + \mathbf{H}_{\mathrm{PG},4:\infty}(f)$, (c) ray-tracing only $\mathbf{H}_{\mathrm{RT},0:3}(f)$, (d) propagation graph only $\mathbf{H}_{\mathrm{PG},4:\infty}(f)$, and (e) ray-tracing only $\mathbf{H}_{\mathrm{RT},0:5}(f)$. The crosses mark the propagation paths' angles and delays simulated with ray-tracing for the respective order of interaction ((a) to (d) third-order and (e) up to fifth-order). The combination of a circle and a cross marks the line-of-sight component.

This article has been accepted for publication in a future issue of this journal, but has not been fully edited. Content may change prior to final publication. Citation information: DOI 10.1109/TAP.2016.2589958, IEEE Transactions on Antennas and Propagation

A. Dispersion in Delay

Referring to Table III, 38% of the measured power is contained in the LOS component; ray-tracing up to third-order interactions covers 63%; and the hybrid model captures 69%. The missing power may be contained in some missing specular components or the simulated ones have too low power, see Fig. 7. Although most of the power is contained in a few deterministic paths, the dispersion in delay is not modelled well considering ray-tracing only. Ray-tracing achieves only 47% of the measured rms delay spread whereas the hybrid model has 96%. Considering that 38% of the total measured power is contained in the simulated LOS component, it becomes clear that the importance of the diffuse tail, with respect to received power and the rms delay spread, is even more pronounced in non-LOS situations.

As expected from the reported rms delay spread values in Table III, it appears from Fig. 7 that the diffuse tails of the delay power spectra of the measurements and the hybrid model coincide. The early "deterministic" peaks, simulated with ray-tracing appear at the same delays as observed in the measurements. However, the power of some of the simulated peaks differs from the measurements. A better calibration of relative electromagnetic properties for some of the materials used in ray-tracing may improve the similarity in power. However, we intentionally did not fine-tune/fit the electromagnetic properties to the measurement data in order to rely only on model predictions.

B. Dispersion in Angle

As mentioned in Section V, the array geometry leads to beamforming results with high sidelobes. Therefore we do not report the narrowband azimuth power spectrum and estimates of the rms angular spread. Instead, we rely on visual comparison between the azimuth-delay power profiles.

When inspecting the azimuth-delay power spectrum estimated from third-order ray-tracing in Fig. 8c, we see that ray-tracing does not capture the diffuse tail and its directional behavior. Even for ray-tracing up to fifth-order, the tail is not covered, see Fig. 8e. This is expected, considering our observations with respect to the delay dispersion. We see from Fig. 8a that the early "deterministic" components up to third-order are a good match in angle and delay. The power of several of the components appears to be stronger in the measurements, see Fig. 8a vs. Fig. 8c. This is similar to what we observed for the delay power spectrum and might be improved with a dedicated calibration procedure for ray-tracing in this environment. The azimuth-delay power spectrum obtained from the measurements exhibits only a few peaks which are not covered by ray-tracing up to third-order interactions. Not covered is one particularly strong peak at approximately -120° and $65\,\mathrm{ns}$. Upon investigation, this strong peak appears to be a propagation path generated by four bounces and is consequently not included when ray-tracing is limited to order three. The path is generated by specular reflections, first on glass (internal wall at $6\,\mathrm{m}$), then the metallic blackboard, glass (window to outside) again, and finally the wall framing the window. Fig. 8e includes this peak.

The azimuth-delay power spectrum obtained from the propagation graph provides the contributions for the diffuse tail, see Fig. 8d. We observe that the diffuse contributions spread out in delay according to the main directions of the scattering vertices provided by ray-tracing, e.g. -150°, -50°, 75°, etc. This is in accordance with previous observations and models proposed in [10], [12], [25] and their respective references.

The results for the hybrid model are shown in Fig. 8b. For a detailed analysis we may consider the delay dispersion in the azimuth range from 50° to 150°. It appears that the hybrid model lacks some power at approx. 100° to provide a better visual fit to the measurements in Fig. 8a. On the other hand around -150°, the simulations exhibit more power in comparison to the measurements. Additionally, the measurements have contributions around -120° following the above mentioned missing component from a fourth-order interaction. In general, our measurements do not show a focus of the delay dispersion to a few main angles as suggested by our simulations and the proposals in [10], [12], [25]. It appears the power is more dispersed in direction. Note that it is clear that the proposed model cannot achieve an exact match of the spectra as i) edges are generated stochastically in the propagation graph and ii) receiving angles are limited to the interaction points considered in ray-tracing. Considering this we perceive the simulated diffuse tail as an overall good representation of the measurements.

VII. Conclusion

In this paper we presented a hybrid model for the simulation of indoor reverberant channels. The hybrid model consists of two parts. Part one is ray-tracing to model deterministic components and part two is the propagation graph which generates the diffuse tail in the channel impulse response. All parameters of the propagation graph are obtained from the environment description via ray-tracing and room electromagnetics. We proposed a method to select the scattering vertices of the graph such that the obtained azimuth-delay power spectrum of the diffuse tail is similar to the one from measurements. The recursive structure of the propagation graph yields an efficient simulation of the diffuse tail. The selection of only the first and last interaction points of ray-tracing allows us to keep the computational complexity low. The usual problem in ray-tracing is the choice of the order of interactions. Different metrics were investigated for this purpose, i.e. received power, mean delay and rms delay spread. We found that ray-tracing up to third-order and the propagation graph from fourth-order to infinity is a sufficient choice for our scenario.

Our simulation results, obtained by prediction only, show good agreement to measurements. In particular the diffuse tail is well predicted with respect to its decay rate and its directional behavior.

This article has been accepted for publication in a future issue of this journal, but has not been fully edited. Content may change prior to final publication. Citation information: DOI 10.1109/TAP.2016.2589958, IEEE Transactions on Antennas and Propagation

APPENDIX A
DEFINITION OF THE PROPAGATION GRAPH'S TRANSFER MATRICES

The transfer matrices are defined in [24] according to

$$\mathbf{D}(f) \in \mathbb{C}^{|\mathcal{V}_\mathrm{r}|\times|\mathcal{V}_\mathrm{t}|} \quad \text{connecting } \mathcal{V}_\mathrm{t} \text{ to } \mathcal{V}_\mathrm{r}, \tag{19}$$

$$\mathbf{R}(f) \in \mathbb{C}^{|\mathcal{V}_\mathrm{r}|\times|\mathcal{V}_\mathrm{s}|} \quad \text{connecting } \mathcal{V}_\mathrm{s} \text{ to } \mathcal{V}_\mathrm{r}, \tag{20}$$

$$\mathbf{T}(f) \in \mathbb{C}^{|\mathcal{V}_\mathrm{s}|\times|\mathcal{V}_\mathrm{t}|} \quad \text{connecting } \mathcal{V}_\mathrm{t} \text{ to } \mathcal{V}_\mathrm{s}, \text{ and} \tag{21}$$

$$\mathbf{B}(f) \in \mathbb{C}^{|\mathcal{V}_\mathrm{s}|\times|\mathcal{V}_\mathrm{s}|} \quad \text{interconnecting } \mathcal{V}_\mathrm{s}, \tag{22}$$

with entries defined as the edge transfer functions in (7). For matrix $\mathbf{B}(f)$,

$$[\mathbf{B}(f)]_{nn'} = \begin{cases} A_e(f), & e = (v_n, v_{n'}) \in \mathcal{E}_\mathrm{s}, \\ 0 & \text{otherwise}, \end{cases} \tag{23}$$

i.e., entry n, n' of $\mathbf{B}(f)$ is the edge transfer function from scatterer vertex v_n to vertex $v_{n'}$ provided edge $(v_n, v_{n'})$ is in the edge set $\mathcal{E}_\mathrm{s}$ and zero otherwise. The matrices $\mathbf{T}(f)$, $\mathbf{R}(f)$ and $\mathbf{D}(f)$ are defined in a similar manner.

APPENDIX B
THE PROPAGATION GRAPH'S APPROXIMATE NUMBER OF COMPONENTS WITH INTERACTION ORDER n

Considering a stochastic edge set generation, we approximate the number of components for one pair of transmitter and receiver vertices for interaction order n. We assume independent generation of edges in $\mathcal{E}_\mathrm{t}$, $\mathcal{E}_\mathrm{s}$, and $\mathcal{E}_\mathrm{r}$ with probability of visibility $P_{\mathrm{vis,t}}$, P_{vis}, and $P_{\mathrm{vis,r}}$, respectively. For zeroth-order, the approximate number of components corresponds to the probability of LOS in the propagation graph. The approximate number for first-order interactions is

$$\mathrm{E}[N_\mathrm{PG}(1)] \approx \mathrm{E}[\mathrm{odi}_{\mathcal{V}_\mathrm{t}}]\, P_{\mathrm{vis,r}}, \tag{24}$$

where $\mathrm{E}[\,\cdot\,]$ is the expectation operator, $\mathrm{E}[\mathrm{odi}_{\mathcal{V}_\mathrm{t}}]$ is the expected number of edges from the transmitter to scatterer vertices which will reach the receiver vertice with $P_{\mathrm{vis,r}}$. The expected number of edges from transmitter to scatterer, also denoted as the mean outdegree of the transmit vertices, is given as $\mathrm{E}[\mathrm{odi}_{\mathcal{V}_\mathrm{t}}] = |\mathcal{V}_\mathrm{s}|\, P_{\mathrm{vis,t}}$. Similarly, we obtain the approximate number of paths for the second-order interaction as

$$\mathrm{E}[N_\mathrm{PG}(2)] \approx \mathrm{E}[\mathrm{odi}_{\mathcal{V}_\mathrm{t}}]\, \mathrm{E}[\mathrm{odi}_{\mathcal{V}_\mathrm{s}}]\, P_{\mathrm{vis,r}}, \tag{25}$$

where $\mathrm{E}[\mathrm{odi}_{\mathcal{V}_\mathrm{s}}]$ is the mean outdegree of scattering vertices (expected number of edges from scatterer to scatterer vertices) with the assumption that the outdegree of all scatterer vertices equals $\mathrm{E}[\mathrm{odi}_{\mathcal{V}_\mathrm{s}}]$ and that the probability of vertices in $\mathcal{V}_\mathrm{s}$ with outdegree of zero can be neglected. For the stochastic edge generation the mean outdegree of scattering vertices reads

$$\mathrm{E}[\mathrm{odi}_{\mathcal{V}_\mathrm{s}}] = (|\mathcal{V}_\mathrm{s}| - 1) P_{\mathrm{vis}}. \tag{26}$$

Considering the recursive structure of the graph, we obtain by extending (25) to the nth-order interaction

$$\mathrm{E}[N_\mathrm{PG}(n)] \approx \mathrm{E}[\mathrm{odi}_{\mathcal{V}_\mathrm{t}}] \mathrm{E}[\mathrm{odi}_{\mathcal{V}_\mathrm{s}}]^{n-1} P_{\mathrm{vis,r}}. \tag{27}$$

We observe that $\mathrm{E}[N_\mathrm{PG}(n)]$ grows exponentially with the number of interactions.

APPENDIX C
ESTIMATION OF THE AZIMUTH-DELAY POWER SPECTRA

Azimuth-delay power spectra are estimated from measurements and simulations. These spectra are obtained by applying the Bartlet beamformer [39] for the virtual receiver array with $A = 175$ antenna elements shown in Fig. 2, at each delay. The three dimensional position vectors of the antennas $\mathbf{r}_a$, indexed with $a = 1 \ldots A$, are relative to the chosen center of the array at antenna position 88 indicated with the red dot in Fig. 2.

We first calculate the discrete channel impulse responses from the channel transfer function similar as in (13) as

$$h_{\mathrm{HY},a}[\ell] = \mathrm{IDFT}\left\{\mathbf{H}_{\mathrm{HY},a}[i]\, W[i]\right\}[\ell]. \tag{28}$$

and define $\mathbf{h}_\mathrm{HY}[\ell] = [h_{\mathrm{HY},1}[\ell], \ldots, h_{\mathrm{HY},A}[\ell]]^T$. In general the discretized azimuth-delay power spectrum is estimated by averaging over the coelevation angles as

$$ADPS_\mathrm{HY}[\ell, q] = \frac{1}{P} \sum_{q'=1}^{Q'} \frac{\mathbf{a}(\phi_{q'}, \theta_q)^H\, \mathbf{h}_\mathrm{HY}[\ell] \mathbf{h}_\mathrm{HY}^H[\ell]\, \mathbf{a}(\phi_{q'}, \theta_q)}{|\mathbf{a}(\phi_{q'}, \theta_q)|^2} \sin(\phi_{q'}), \tag{29}$$

with the array steering vector

$$\mathbf{a}(\phi_{q'}, \theta_q) = [e^{j\frac{2\pi}{\lambda}\mathbf{e}(\phi_{q'},\theta_q)\cdot\mathbf{r}_1}, \ldots, e^{j\frac{2\pi}{\lambda}\mathbf{e}(\phi_{q'},\theta_q)\cdot\mathbf{r}_A}]^T, \tag{30}$$

and the direction vector

$$\mathbf{e}(\phi_{q'}, \theta_q) = [\cos(\theta_q)\sin(\phi_{q'}), \sin(\theta_q)\sin(\phi_{q'}), \cos(\phi_{q'})]^T. \tag{31}$$

The coelevation ϕ is indexed with q', the azimuth angle θ is indexed with q and λ is the wavelength. In the presented results of Fig. 8 we select the coelevation equal to 90°. Considering an interval for the coelevation showed no major differences in the spectra except that the azimuthal concentration of the lobes was less. This dispersion of the power makes it slightly more difficult to discern peaks and thus we consider only a single coelevation angle.

REFERENCES

[1] P. Almers, E. Bonek, A. Burr, N. Czink, M. Debbah, V. Degli-Esposti, H. Hofstetter, P. Kyösti, D. Laurenson, G. Matz, A. Molisch, C. Oestges, and H. Özcelik, "Survey of Channel and Radio Propagation Models for Wireless MIMO Systems," *EURASIP J. on Wireless Commun. and Netw.*, vol. 2007, p. 19, 2007.

[2] J. Kunisch and J. Pamp, "Measurement results and modeling aspects for the UWB radio channel," in *Ultra Wideband Systems and Technologies, 2002. Digest of Papers. 2002 IEEE Conf. on*, May 2002, pp. 19–24.

[3] A. Richter, J. Salmi, and V. Koivunen, "Distributed Scattering in Radio Channels and its Contribution to MIMO Channel Capacity," in *Antennas and Propagation, 2006. EuCAP 2006. First European Conference on*, 2006, pp. 1–7.

[4] A. Richter, "The Contribution of Distributed Scattering in Radio Channels to Channel Capacity: Estimation and Modeling," in *Signals, Systems and Computers, 2006. ACSSC '06. Fortieth Asilomar Conference on*, 2006, pp. 951–955.

[5] F. Quitin, C. Oestges, F. Horlin, and P. De Doncker, "Diffuse Multipath Component Characterization for Indoor MIMO Channels," in *Antennas and Propagation (EuCAP), 2010 Proceedings of the Fourth European Conference on*, 2010, pp. 1–5.

[6] N. Czink, A. Richter, E. Bonek, J.-P. Nuutinen, and J. Ylitalo, "Including Diffuse Multipath Parameters in MIMO Channel Models," in *Proc. of the 66th IEEE Veh. Technol. Conf. (VTC)*, A. Richter, Ed., 2007, pp. 874–878.

This article has been accepted for publication in a future issue of this journal, but has not been fully edited. Content may change prior to final publication. Citation information: DOI 10.1109/TAP.2016.2589958, IEEE Transactions on Antennas and Propagation

[7] M. Landmann, M. Kaeske, R. Thoma, J. Takada, and I. Ida, "Measurement Based Parametric Channel Modeling Considering Diffuse Scattering and Specular Components," in *International Symposium on Antennas and Propagation*, Niigata, Japan, Aug. 2007, pp. 1–5.

[8] G. Steinböck, T. Pedersen, B. Fleury, W. Wang, and R. Raulefs, "Distance Dependent Model for the Delay Power Spectrum of In-room Reverberant Channels," *IEEE Trans. Antennas Propagat.*, vol. 61, no. 8, pp. 4327 – 4340, Aug. 2013.

[9] J. Andersen, J. Nielsen, G. Pedersen, G. Bauch, and J. Herdin, "Room Electromagnetics," *IEEE Antennas Propag. Mag.*, vol. 49, no. 2, pp. 27–33, 2007.

[10] F. Mani, F. Quitin, and C. Oestges, "Directional spreads of dense multipath components in indoor environments: Experimental validation of a ray-tracing approach," *Antennas and Propagation, IEEE Transactions on*, vol. 60, no. 7, pp. 3389 – 3396, July 2012.

[11] E. Leitinger, P. Meissner, C. Rüdisser, G. Dumphart, and K. Witrisal, "Evaluation of position-related information in multipath components for indoor positioning," *IEEE J. Sel. Areas Commun.*, vol. 33, no. 11, pp. 2313–2328, Nov. 2015.

[12] J. Kunisch and J. Pamp, "An ultra-wideband space-variant multipath indoor radio channel model," in *Ultra Wideband Systems and Technologies, 2003 IEEE Conf. on*, Nov. 2003, pp. 290–294.

[13] J. Jarvelainen, K. Haneda, M. Kyro, V.-M. Kolmonen, J. Takada, and H. Hagiwara, "60 GHz radio wave propagation prediction in a hospital environment using an accurate room structural model," in *Antennas and Propagation Conference (LAPC), 2012 Loughborough*, 2012, pp. 1–4.

[14] P. Meissner, M. Gan, F. Mani, E. Leitinger, M. Froehle, C. Oestges, T. Zemen, and K. Witrisal, "On the Use of Ray Tracing for Performance Prediction of UWB Indoor Localization Systems," in *IEEE ICC 2013 Workshop on Advances in Network Localization and Navigation (ANLN)*, Budapest, Hungary, 2013.

[15] V. Degli-Esposti, "A Diffuse Scattering Model for Urban Propagation Prediction," *IEEE Trans. Antennas Propag.*, vol. 49, no. 7, pp. 1111–1113, 2001.

[16] V. Degli-Esposti, D. Guiducci, A. de'Marsi, P. Azzi, and F. Fuschini, "An Advanced Field Prediction Model Including Diffuse Scattering," *IEEE Trans. Antennas Propag.*, vol. 52, no. 7, pp. 1717–1728, 2004.

[17] V. Degli-Esposti, F. Fuschini, E. M. Vitucci, and G. Falciasecca, "Measurement and Modelling of Scattering From Buildings," *IEEE Trans. Antennas Propag.*, vol. 55, no. 1, pp. 143–153, 2007.

[18] E. M. Vitucci, F. Mani, V. Degli-Esposti, and C. Oestges, "Polarimetric Properties of Diffuse Scattering From Building Walls: Experimental Parameterization of a Ray-Tracing Model," *IEEE Trans. Antennas Propag.*, vol. 60, no. 6, pp. 2961–2969, 2012.

[19] G. Steinböck, T. Pedersen, B. Fleury, W. Wang, and R. Raulefs, "Experimental Validation of the Reverberation Effect in Room Electromagnetics," *IEEE Trans. Antennas Propagat.*, vol. 63, no. 5, to appear, 2015.

[20] C. Holloway, M. Cotton, and P. McKenna, "A Aodel for Predicting the Power Delay Profile Characteristics Inside a Room," *IEEE Trans. Veh. Technol.*, vol. 48, no. 4, pp. 1110–1120, 1999.

[21] D. Hill, "A Reflection Coefficient Derivation for the Q of a Reverberation Chamber," *IEEE Trans. Electromagn. Compat.*, vol. 38, no. 4, pp. 591–592, 1996.

[22] D. A. Hill, *Electromagnetic Fields in Cavities: Deterministic and Statistical Theories*, ser. IEEE Press Series on Electromagnetic Wave Theory. Piscataway, NJ: Wiley/IEEE Press, 2009.

[23] M. Janson, "Hybride Funkkanalmodellierung für ultrabreitbandige MIMO-Systeme," Ph.D. dissertation, Karlsruher Institut für Technologie, Fakultät für Elektrotechnik and Informationstechnik, Dec. 2010.

[24] T. Pedersen, G. Steinböck, and B. Fleury, "Modeling of Reverberant Radio Channels Using Propagation Graphs," *IEEE Trans. Antennas Propag.*, vol. 60, no. 12, pp. 5978–5988, Dec. 2012.

[25] J. Poutanen, J. Salmi, K. Haneda, V. M. Kolmonen, and P. Vainikainen, "Angular and shadowing characteristics of dense multipath components in indoor radio channels," *IEEE Trans. Antennas Propag.*, vol. 59, no. 1, pp. 245–253, Jan. 2011.

[26] M. Gan, P. Meissner, F. Mani, E. Leitinger, M. Frohle, C. Oestges, K. Witrisal, and T. Zemen, "Calibration of indoor UWB sub-band divided ray tracing using multiobjective simulated annealing," in *Communications (ICC), 2014 IEEE International Conference on*, Jun. 2014, pp. 4844–4849.

[27] F. Mani, F. Quitin, and C. Oestges, "Accuracy of depolarization and delay spread predictions using advanced ray-based modeling in indoor scenarios," *EURASIP Jounal in Wireless Commmunications and Networking*, vol. 2011, p. 11, 2011.

[28] S. U. Inan and S. A. Inan, *Electromagnetic Waves*. Prentice, 2000.

[29] R. Luebbers, "Finite conductivity uniform GTD versus knife edge diffraction in prediction of propagation path loss," *Antennas and Propagation, IEEE Transactions on*, vol. 32, no. 1, pp. 70 – 76, Jan. 1984.

[30] M. Gan, X. Li, F. Tufvesson, and T. Zemen, "Low-Complexity Sub-band Divided Ray Tracing for UWB Indoor Channels," in *31st URSI General Assembly and Scientific Symposium (URSI GASS)*, Beijing, China, Aug. 2014.

[31] R. Diestel, *Graph Theory*. Springer-Verlag, 2000.

[32] B. Montenegro, B. Clerckx, D. Vanhoenacker-Janvier, and C. Oestges, "Literature review and preliminary models for propagation into buildings and forests," Sensor for Terrestrial and Airborne Radio transmitter Rescue Search-STARRS Project, Tech. Rep. IST 2005 33742 UCL DR D 3.1, FP6/2005/IST/5 Contract No. 33742, Dec. 2007.

[33] A. Bamba, M.-T. Martinez-Ingles, D. Gaillot, E. Tanghe, B. Hanssens, J.-M. Molina-Garcia-Pardo, M. Lienard, L. Martens, and W. Joseph, "Experimental investigation of electromagnetic reverberation characteristics as a function of uwb frequencies," *IEEE Antennas Wireless Propag. Lett.*, vol. 14, pp. 859–862, 2015.

[34] W. C. Sabine, *Collected papers on acoustics*. Cambridge: Harvard University Press, 1922.

[35] C. F. Eyring, "Reverberation Time in "Dead" Rooms," *J. Acoust. Soc. Am.*, vol. 1, no. 2A, pp. 217–241, Jan. 1930. [Online]. Available: http://link.aip.org/link/?JAS/1/217/1

[36] P. Meissner, E. Leitinger, M. Lafer, and K. Witrisal, "MeasureMINT UWB database," www.spsc.tugraz.at/tools/UWBmeasurements, 2013. [Online]. Available: www.spsc.tugraz.at/tools/UWBmeasurements

[37] P. Meissner, E. Leitinger, and K. Witrisal, "UWB for Robust Indoor Tracking: Weighting of Multipath Components for Efficient Estimation," *IEEE Wireless Communications Letters*, vol. 3, no. 5, pp. 501–504, Jul. 2014.

[38] P. Meissner, E. Leitinger, M. Lafer, and K. Witrisal, "Real-Time Demonstration System for Multipath-Assisted Indoor Navigation and Tracking (MINT)," in *IEEE ICC 2014 Workshop on Advances in Network Localization and Navigation (ANLN)*, Sydney, Australia, 2014.

[39] H. Krim and M. Viberg, "Two decades of array signal processing research: the parametric approach," *IEEE Signal Process. Mag.*, vol. 13, no. 4, pp. 67–94, Jul. 1996.

Gerhard Steinböck received the DI (FH) degree in telecommunications from Technikum Wien, Austria in 1999. From 2000 to 2006, he worked as a R&D engineer at the Austrian Institute of Technology (AIT), Vienna, Austria, contributing among other things in the hard- and software development of a real-time radio channel emulator. Gerhard Steinböck received the M.Sc.E. *(cum laude)* degree in wireless communications in 2008 and the Ph.D. degree in wireless communications in 2013 from Aalborg University, Denmark. Since 2013 he is a postdoctoral researcher at Aalborg University. His research interests lie in the area of wireless communications, radio channel modeling, radio channel estimation and sounding, and radio geolocation techniques.

This article has been accepted for publication in a future issue of this journal, but has not been fully edited. Content may change prior to final publication. Citation information: DOI 10.1109/TAP.2016.2589958, IEEE Transactions on Antennas and Propagation

Mingming Gan (S'11) received the B.Sc. degree in electronic information engineering from Minzu University of China, China in 2007. She received the M.Sc. degree in wireless communications from Lund University, Sweden in 2010, with her Master Thesis written at the FTW Telecommunications Research Center Vienna, Austria. In 2015, she received her Ph.D. degree with distinction in engineering sciences from Vienna University of Technology, Austria. From 2010 to 2015, she was with the FTW Telecommunications Research Center Vienna working as a researcher in the "Signal and Information Processing" department. Her research interests are in the fields of modelling of wireless propagation channels, indoor channel characterization for high-speed short-range systems, time-variant vehicle-to-vehicle channel characterization, time-variant fast fading statistics and diffuse scattering algorithms. She is currently working at AIT Austrian Institute of Technology as a researcher in the research group for ultra-reliable wireless machine-to-machine communications.

Paul Meissner (S'10–M'15) was born in Graz, Austria, in 1982. He received the B.Sc. and Dipl.-Ing. degree (with distinction) in information and computer engineering from Graz University of Technology, Graz, Austria in 2006 and 2009, respectively. He received the Ph.D. degree in electrical engineering (with distinction) from the same university in 2014.

Paul has been a postdoctoral researcher at the Signal Processing and Speech Communication Laboratory (SPSC) of Graz University of Technology, Graz, Austria. His research topics include statistical signal processing, localization, estimation theory and propagation channel modeling. He served in the TPC of the IEEE Workshop on Advances in Network Localization and Navigation (ANLN) at the IEEE Intern. Conf. on Communications (ICC) 2015 and of IEEE RFID 2015.

Erik Leitinger was born in Graz, Austria, in 1985. He received the B.Sc and Dipl.-Ing. degree in electrical engineering (with highest honors) in 2012 and the Dr.techn. degree (Ph.D.) (with highest honors) in 2016 from Graz University of Technology, Austria.

Erik is currently a postdoctoral researcher at the Signal Processing and Speech Communication Laboratory (SPSC) of Graz University of Technology, Graz, Austria. His research topics include statistical signal processing, Bayesian inference, localization, estimation theory, channel modeling and cognitive control.

Klaus Witrisal (S'98–M'03) received the Dipl.-Ing. degree in electrical engineering from Graz University of Technology, Graz, Austria, in 1997, the Ph.D. degree (cum laude) from Delft University of Technology, Delft, The Netherlands, in 2002, and the Venia Docendi (Habilitation) from Graz University of Technology in 2009.

He is currently an Associate Professor at the Signal Processing and Speech Communication Laboratory (SPSC) of Graz University of Technology, Graz, Austria, where he has been participating in various national and European research projects focused on wireless communications and positioning. He was a co-chair of the Technical Working Group "Indoor" of the COST Action IC1004 "Cooperative Smart Radio Communications for Green Smart Environments" and he currently chairs the experimental working group "Localization and Tracking" in the COST action IRACON "Inclusive Radio Communications". His research interests are in signal processing for wireless communications, propagation channel modeling, and positioning.

Prof. Witrisal served as a leading chair for the IEEE Workshop on Advances in Network Localization and Navigation (ANLN) at the IEEE Intern. Conf. on Communications (ICC) 2013–2016 and for the IEEE International Workshop on Localization and Tracking: Indoors, Outdoors, and Emerging Networks (LION) at GLOBECOM 2015 and 2016, as a TPC co-chair and chair of the Workshop on Positioning, Navigation and Communication (WPNC) 2011, 2014, and 2015, and as a co-organizer of the Workshop on Localization in UHF RFID at the IEEE 5th Annual Intern. Conf. on RFID, 2011. He is an associate editor of IEEE Communications Letters since 2013. From 2007 to 2011, he was a co-chair of the MTT/COM Chapter of IEEE Austria.

Thomas Zemen (S'03–M'05–SM'10) received the Dipl.-Ing. degree (with distinction) in electrical engineering in 1998, the doctoral degree (with distinction) in 2004 and the Venia Docendi (Habilitation) for "Mobile Communications" in 2013, all from Vienna University of Technology. From 1998 to 2003 he worked as Hardware Engineer and Project Manager for the Radio Communication Devices Department, Siemens Austria. From 2003 to 2015 Thomas Zemen was with FTW Telecommunications Research Center Vienna and Head of the "Signal and Information Processing" department since 2008. Since 2014 Thomas Zemen has been Senior Scientist at AIT Austrian Institute of Technology leading the research group for ultra-reliable wireless machine-to-machine communications. He is the author or coauthor of four book chapters, 30 journal papers and more than 80 conference communications. His research interests focus on reliable, low-latency wireless communications for highly autonomous vehicles; sensor and actuator networks; vehicular channel measurements and modeling; time-variant channel estimation; cooperative communication systems and interference management. Dr. Zemen is an External Lecturer with the Vienna University of Technology and serves as Editor for the IEEE Transactions on Wireless Communications.

Troels Pedersen received the M.Sc.E. degree in digital communications and the Ph.D. degree in wireless communications from Aalborg University, Denmark, in 2004 and 2009, respectively. Since 2009 he has been with the Department of Electronic Systems, Aalborg University, first as assistant professor and since 2012 as associate professor. He received the "Teacher of the Year 2011" award by the Study Board for Electronics and IT, Aalborg University. In Spring 2012 he was a visiting professor at IETR, University Rennes 1, France. His research interests lie in the area of statistical signal processing and communication theory, including sensor array signal processing, radio geolocation techniques, radio channel modeling, and radio channel sounding.